RSC Advances

PAPER

View Article Online
View Journal | View Issue

Cite this: *RSC Adv.*, 2020, **10**, 26246

Nano-MOF@defected film C_3N_4 Z-scheme composite for visible-light photocatalytic nitrogen fixation†

Zhu Ding, Shuo Wang, Xue Chang, Dan-Hong Wang* and Tianhao Zhang*

Received 21st April 2020
Accepted 3rd July 2020

DOI: 10.1039/d0ra03562a

rsc.li/rsc-advances

Photocatalytic nitrogen fixation has attracted extensive attention in recent years. Studies have shown that catalytic materials with O, N and other defects can effectively reduce the bond energy of N≡N triple bond when N_2 is adsorbed on the defects. As an outstanding non-metallic catalyst, g-C_3N_4 has been widely studied in the field of photocatalytic catalysis, and the nitrogen-defected C_3N_4 shows promoted photocatalytic activity. Herein, nano-size MOF-74 particles (<20 nm) was dispersed on nitrogen-defected C_3N_4 thin film (~4 nm) *via* a simple sol–gel method. The combination of Nano-MOF and defected film C_3N_4 could effectively improve the photocatalytic activity of nitrogen fixation through Z-scheme mechanism compared with pure defected film C_3N_4.

1. Introduction

As an indispensable energy source, ammonia plays an important role in industry and agriculture.[1–3] Ammonia is even called "the other hydrogen" in the fuel world.[4] The process of ammonia synthesis consumes a huge amount of energy (1–2% of the total world energy consumption) every year, accompanying serious environmental pollution.[5,6] Photocatalytic technology can directly convert solar energy into chemical energy.[7] In recent years, photocatalytic nitrogen fixation has been widely studied because of its simple reaction conditions, clean and pollution-free reaction process and other advantages.[8] However, due to the low utilization rate of visible light and the high recombination rate of photogenic carriers, the photocatalytic activity for nitrogen fixation is relatively poor.[9] At the same time, N_2 molecules involved in the reaction are relatively stable and difficult to dissociate due to the N≡N triple bond, which shows chemical reaction inertia and poor proton affinity, thus preventing electron transport and Lewis acid–base reaction.[10] This poses a serious challenge to photocatalytic materials.[11] How to improve the utilization rate of visible light, reduce the recombination of photogenic carriers and weaken the N≡N triple bond has become the key to improve the activity of photocatalytic nitrogen fixation.[12]

On account of the high porosity and compatibility, metal–organic frameworks (MOFs) have been studied extensively in the field of photocatalysis in recent years.[13,14] The unique properties of MOFs make it convenient to combine with other catalytic materials,[15] thus forming new functional composite materials.[16] MOFs' channel has a certain adsorption effect on water-soluble nitrogen in water, so as to shorten the distance between water-soluble nitrogen and catalytic sites, and further to weaken the bond energy of N≡N triple bond.[17,18] However, MOFs show poor catalytic capacity,[19] so they need to be modified or compounded with other active materials to improve photocatalytic activity. For a long time, there has been no in-depth study on the particle size of MOFs,[20] and most of them are single crystal with large size (~μm), and only a handful of MOFs exist in the form of polycrystalline powder due to its synthesis, but most of them are about hundreds of nanometers in size.[21] As a result, a majority of the MOFs cannot be well compounded and interact with other materials, so their performances will not be improved. For example, Zn-MOF-74 has the advantages of high stability and high gas absorption capacity.[22] However, the single crystal size of Zn-MOF-74 is more than ten to dozens of microns, so large-sized Zn-MOF-74 is difficult to be well combined with some other morphological materials, such as sheet materials.

g-C_3N_4 is also an excellent catalytic material,[23] which has been widely used in the field of photocatalysis due to its π-conjugate electron structure, appropriate bandgap width, stable chemical properties and low synthesis cost.[24] It has been reported that g-C_3N_4 with nitrogen vacancy has good photocatalytic nitrogen fixation performance, so the combination of MOFs and defected g-C_3N_4 may have a good synergistic effect.[25,26] So far, people have tried to compound g-C_3N_4 with ZIF-8,[27,28] UiO-66,[29,30] MIL[31,32] and other MOFs to form some binary heterojunction composite materials.[33] It can take the complementary advantages of both MOFs and g-C_3N_4, overcome their shortcomings and enhance their photocatalytic

School of Materials Science and Engineering, School of Physics, Tianjin Key Laboratory of Photonics Materials and Technology for Information Science, Nankai University, Tianjin 300350, China. E-mail: zhangth@nankai.edu.cn

† Electronic supplementary information (ESI) available. See DOI: 10.1039/d0ra03562a

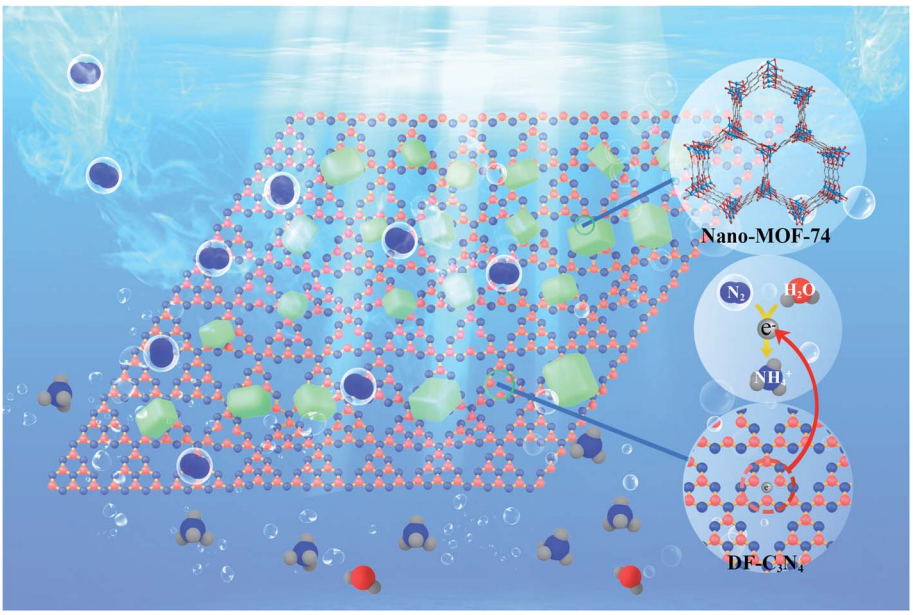

Scheme 1 Nano-MOF@defected film C_3N_4 composite for visible-light photocatalytic nitrogen fixation mechanism.

activity to some extent.[34,35] However, the particle size of traditional bulk g-C_3N_4 is also quite large, and when it is combined with large-sized MOFs, the interaction between them is very weak and there is no good synergistic effect. How to better compound MOFs with g-C_3N_4 is still of great research significance.[36,37] In this work, the particle size of Zn-MOF-74 was achieved to be <20 nm on average, and g-C_3N_4 is peeled to get thin film (~4 nm), so that the nanoparticle MOF (Nano-MOF-74) can be easily dispersed on thin film g-C_3N_4 (F-C_3N_4). Further, the Nano-MOF-74 can be combined with nitrogen-defected thin film of g-C_3N_4 (DF-C_3N_4) to form Z-scheme composite (MOF@DF-C_3N_4) (Scheme 1). It was found that the MOF@DF-C_3N_4 composite could effectively improve its photocurrent and photocatalytic activity of nitrogen fixation compared with pure DF-C_3N_4, and its visible photocatalytic nitrogen fixation yield could reach 2.32 mmol g^{-1} h^{-1}.

2. Results and discussion

The comparison of photocatalytic nitrogen fixation activity on different catalysts shows that (Fig. 1a) pure Nano-MOF-74(Zn) has basically no visible light catalytic activity, and the visible light activity for F-C_3N_4 is relatively low. After the combination of Nano-MOF-74 and F-C_3N_4, the photocatalytic activity is improved to a certain extent, about 2.2 times that of F-C_3N_4, which indicates that the combination of Nano-MOF-74 and F-C_3N_4 can improve the photocatalytic activity. When F-C_3N_4 is made into nitrogen-defected DF-C_3N_4, its visible light catalytic activity increases significantly. This is due to the existence of nitrogen defects, which can adsorb N_2 and reduce the bond energy of N≡N triple bond. Moreover, nitrogen defects can capture photogenic electrons and thus hinder photogenic carrier recombination.[38] After the combination of Nano-MOF-74 and DF-C_3N_4, its photocatalytic nitrogen fixation activity was greatly improved, which was about 2.3 times higher than that of pure DF-C_3N_4 after 2 h′ light irradiation. According to the results, both F-C_3N_4 and DF-C_3N_4 have a good synergistic effect with Nano-MOF-74 and can effectively improve photocatalytic nitrogen fixation activity. At the same time, we conducted relevant experiments to prove its catalytic model (Fig. S1†). According to the activity analysis of the catalyst under light irradiation and no light irradiation, there was no ammonia nitrogen formation in the absence of light, so we considered its catalytic mode as photocatalysis model. The blank visible light photocatalytic experiments on DF-C_3N_4 are also conducted under Ar and air atmosphere respectively to eliminate the decomposition of DF-C_3N_4 (Fig. S2†). The reason for using full light spectrum irradiation is to increase its photocatalytic activity to make the contrast more obvious. Ar with a flow rate of 30 ml min^{-1} was introduced in the sealed reaction solution for 60 min to eliminate the water-soluble N_2. The visible light catalytic nitrogen fixation activity is very low under Ar atmosphere. This result also indicates that the nitrogen fixation photocatalytic activity obtained under air atmosphere on DF-C_3N_4 comes from the decomposition of water-soluble N_2.

Fig. 1b shows the visible light photocurrent of different catalysts. It can be seen that the photocatalytic nitrogen fixation activity corresponds to the order of the photocurrent. On the one hand, photocurrent is related to the photocarrier concentration of the catalyst, on the other hand, it is related to the recombination of electrons and holes. When the catalysts are exposed to the visible light, the photocurrent of MOF@DF-C_3N_4 is the highest. This result indicates that the combination of Nano-MOF-74 with DF-C_3N_4 can effectively reduce the recombination of photogenic electrons and holes and improve the photocarrier concentration. The photocurrent of DF-C_3N_4 under the visible light irradiation is improved compared with F-C_3N_4, which indicates that the existence of nitrogen defects can

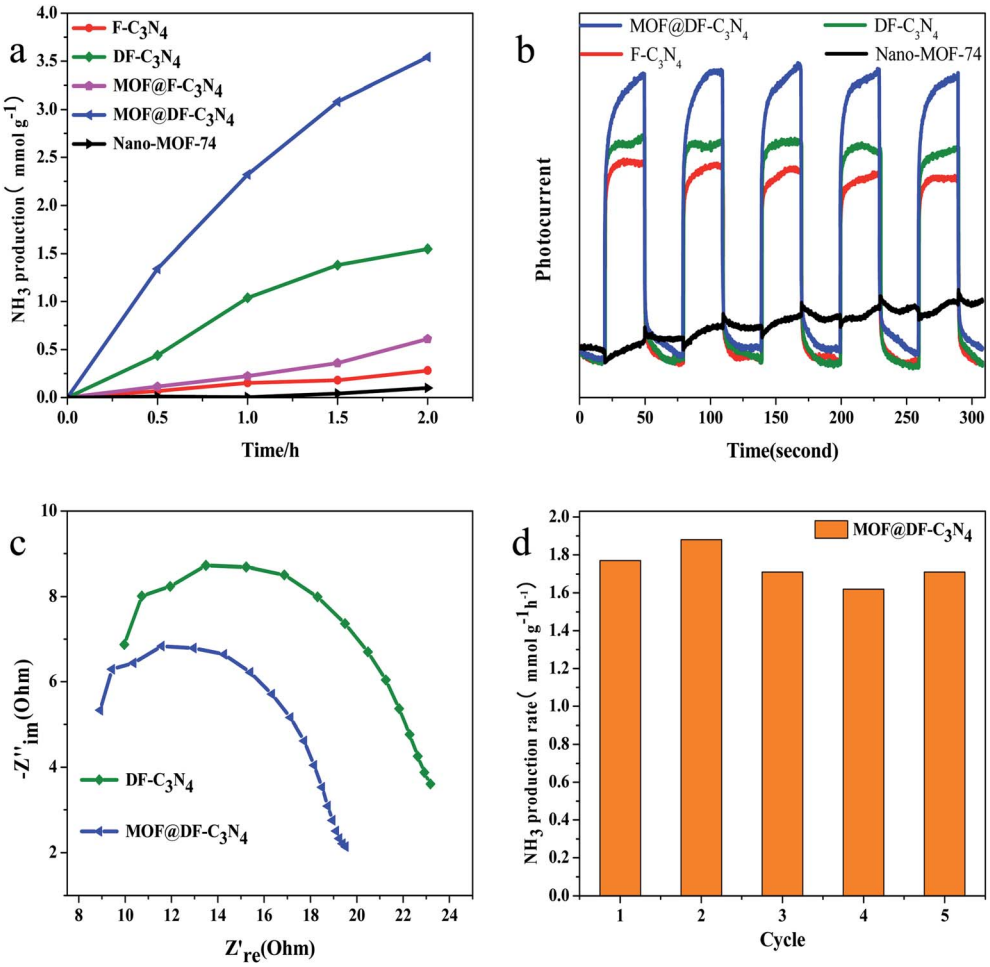

Fig. 1 (a) Photocatalytic nitrogen fixation activity for different catalysts under the visible light. (b) The visible light photocurrent for different catalysts. (c) EIS spectra of as-prepared catalysts under visible light irradiation. (d) Photocatalytic ammonia production rates in the first 2 h for cyclic tests of MOF@DF-C_3N_4.

improve the separation ability of photocarriers. As shown in Fig. 1c, compared with pure DF-C_3N_4, the MOF@DF-C_3N_4 composite catalyst showed the smaller Nyquist radius, which means the lower charge transfer resistance under the visible light. The low electrical resistance between interfaces is beneficial to the charge transfer and the separation of photogenic

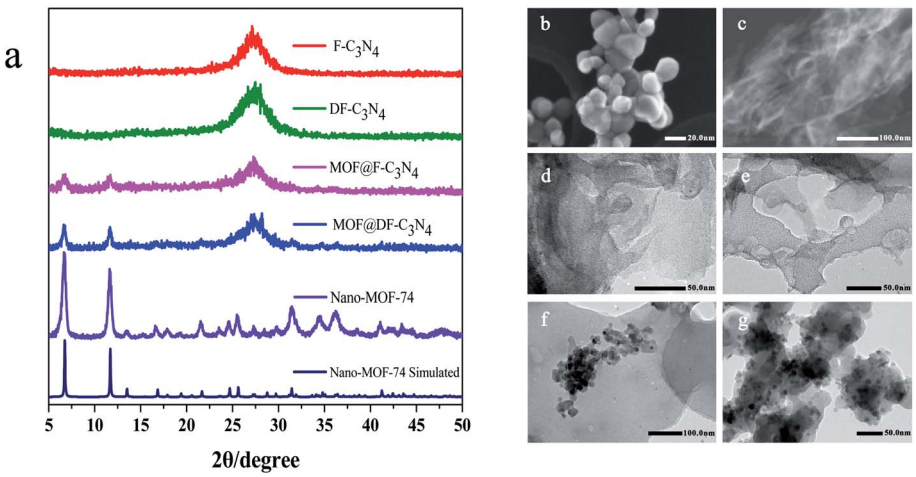

Fig. 2 (a) X-ray diffraction patterns of the samples and STEM images of (b) Nano-MOF-74, (c) DF-C_3N_4 and TEM images of (d) F-C_3N_4, (e) DF-C_3N_4, (f) MOF@F-C_3N_4, (g) MOF@DF-C_3N_4.

electrons and holes. As shown in Fig. 1d, the ammonia production rate is well maintained during five cyclic tests with each run for 2 h. So it can be seen that the catalyst has good reusability and stability.

Fig. 2a shows X-ray diffraction patterns of the composites. Nano-MOF-74 has two main peaks at 6.7° and 11.6° respectively, which is consistent with bulk MOF-74 as shown Fig. S3.† For MOF@F-C_3N_4 and MOF@DF-C_3N_4 composites, the two main peaks of MOF-74 can still be seen, along with the diffraction peak (002) of g-C_3N_4, indicating that the two materials of Nano-MOF-74 and g-C_3N_4 have been successfully combined together. Through STEM dark field image as shown in Fig. 2b and c, we can clearly see the morphology of Nano-MOF-74 and DF-C_3N_4 (SEM images are shown in Fig. S4†). The particle size of Nano-MOF-74 is <20 nm, which is quite different from the traditional bulk Zn-MOF-74 with a size of ten to dozens of microns. Both F-C_3N_4 and DF-C_3N_4 show thin film morphology according to TEM images (Fig. 2d and e). AFM images (Fig. 3) show that F-C_3N_4 thin film presents a thickness of ~4 nm compared with bulk C_3N_4 (~40 nm). The thin film shows a better morphology and is more conducive to form the composite with Nano-MOF-74. From TEM images for the composites (Fig. 2f and g), we can see that Nano-MOF-74 can be well dispersed on F-C_3N_4 and DF-C_3N_4 with a nanosize <20 nm. In accordance with TEM element mapping images for the composites (Fig. S5 and S6†), Zn element is distributed in the nanoparticles and N element is distributed in the nanosheets, indicating the successful combination of Nano-MOF-74 and thin film g-C_3N_4. Moreover, Nano-MOF-74 did not form a wrapping state with C_3N_4, but dispersed and attached onto the surface of C_3N_4. If the proportion of Nano-MOF-74 is too high, it will cover the surface photoactive sites of thin film C_3N_4 and hinder the irradiation of light on thin film C_3N_4, thus decreasing the photoactivity of nitrogen

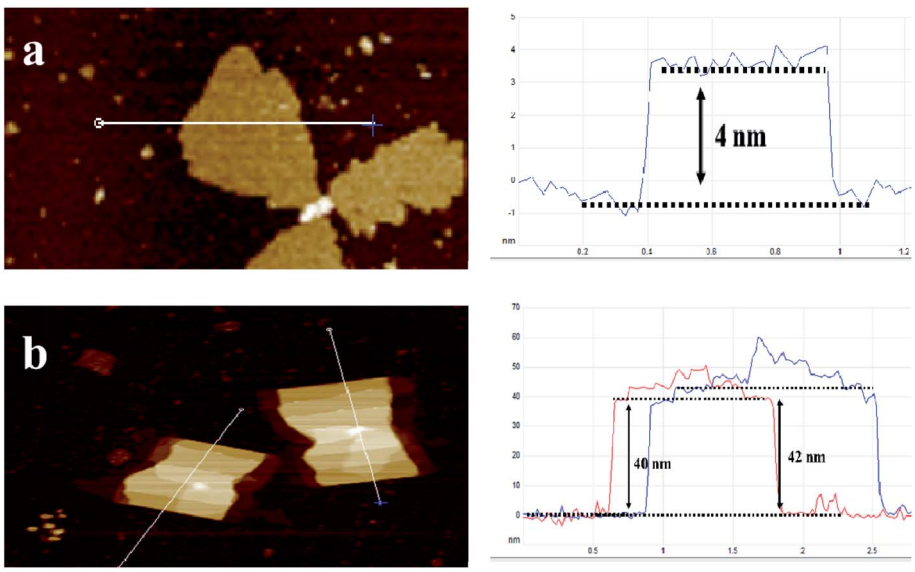

Fig. 3 AFM images of F-C_3N_4 (a) and bulk C3N4 (b).

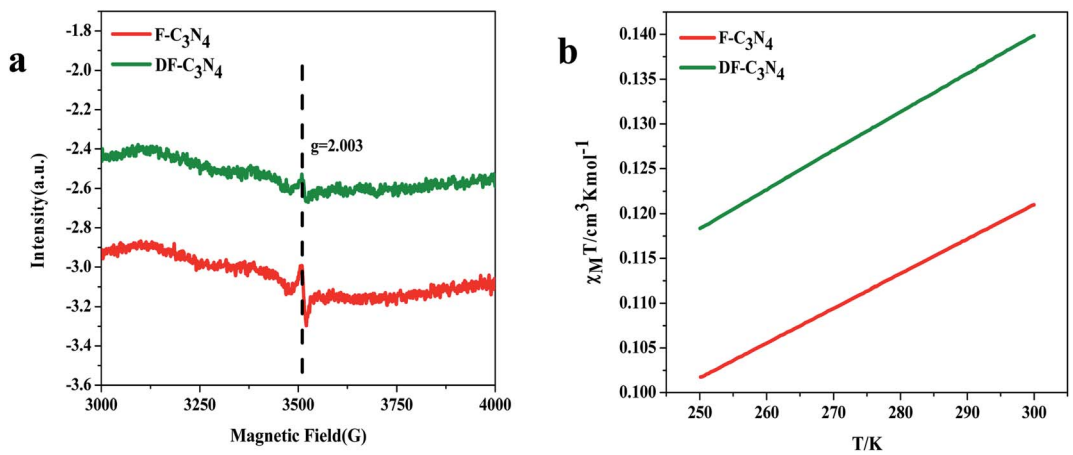

Fig. 4 ESR results for F-C_3N_4 and DF-C_3N_4 (a) and temperature dependent molar magnetic susceptibility $\chi_m T$ for F-C_3N_4 and DF-C_3N_4 (b).

fixation. Therefore, the combination of a small amount of Nano-MOF-74 (20 wt%) and thin film C_3N_4 (80 wt%) does not affect the light absorption of thin film C_3N_4 and increase its photoactivity when they interact with each other.

Elemental analysis was used to determine the C/N molar ratio in F-C_3N_4 and DF-C_3N_4 and to determine the type of defects formed in the DF-C_3N_4 framework (Table S1†). The C/N molar ratio of DF-C_3N_4 was 0.68 (the mass ratio of C is 33.93% and N is 57.95%), which was higher than that of F-C_3N_4 (0.66, the mass ratio of C is 33.56% and N is 58.84%). This finding indicates that the defects formed in the DF-C_3N_4 framework were nitrogen vacancies with electrons trapped in as shown in eqn (1). The electrons delocalized in nitrogen vacancies are suggested to play an important role in nitrogen fixation. Thus DF-C_3N_4 shows higher photocatalytic activity than F-C_3N_4 as shown in Fig. S9.† The unpaired electrons at $g = 2.003$ were detected for both F-C_3N_4 and DF-C_3N_4 by ESR as shown in Fig. 4a, suggesting the formation of nitrogen vacancies with electrons trapped in. Magnetic susceptibility measurements (Fig. 4b) also proved that an increase in magnetic susceptibility ($\chi_m T$) is observed for DF-C_3N_4 compared that for F-C_3N_4, suggesting the formation of more unpaired electrons captured by nitrogen vacancies for DF-C_3N_4 than that for F-C_3N_4.

$$C_3N_4 \rightarrow C_3N_{4-x} + xV_N^{\cdots} + 3xe + \frac{x}{2}N_2 \quad (1)$$

Fig. 5a shows the UV-Vis light absorption spectra of the photocatalysts. The strongest absorption peak of F-C_3N_4, DF-C_3N_4, MOF@F-C_3N_4 and MOF@DF-C_3N_4 is at 380 nm, and the strongest absorption peak of Nano-MOF-74 is at 400 nm, which are caused by the band transition of the semiconductors. The absorption edge of F-C_3N_4 is at 450 nm, and F-C_3N_4 basically has no absorption in the visible light region after 450 nm. Compared with F-C_3N_4, the absorption of DF-C_3N_4, MOF@F-C_3N_4 and MOF@DF-C_3N_4 have different degrees of redshift. Especially, when Nano-MOF-74 was combined with DF-C_3N_4 to obtain MOF@DF-C_3N_4, the absorption in the visible light region was significantly increased, which was also the main reason for the increase in the visible light nitrogen fixation activity. Fig. 5b shows the Kubelka–Munk plots converted from the UV-Vis DRS spectra. The calculated bandgaps for F-C_3N_4, DF-C_3N_4, MOF@F-C_3N_4 and MOF@DF-C_3N_4 are 2.76, 2.68, 2.71 and 2.65 eV, respectively (Table 1). Compared with F-C_3N_4 or DF-C_3N_4, after combining with Nano-MOF-74, the bandgaps of the composites decrease to a certain extent, which is more conducive to the absorption of visible light. Compared with F-C_3N_4, the narrower energy gap for DF-C_3N_4 can be explained by the formation of

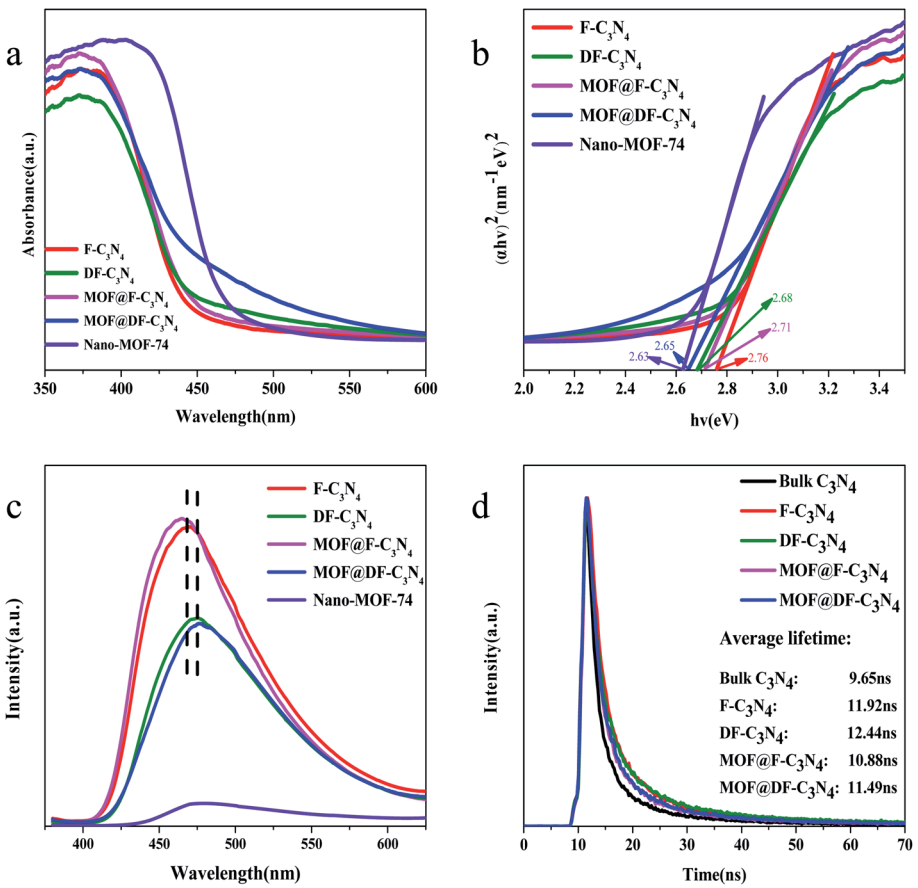

Fig. 5 (a) UV-Vis light absorption spectra of the photocatalysts; (b) Kubelka–Munk plots converted from the UV-Vis DRS spectra; (c) steady state PL spectra of the photocatalysts and (d) room temperature transient state fluorescence spectra for the photocatalysts.

Table 1 The energy gap and average lifetime of different photocatalysts

Sample	E_g (eV)	Average lifetime (ns)
Bulk C_3N_4	2.62	9.65
F-C_3N_4	2.76	11.92
DF-C_3N_4	2.68	12.44
MOF@F-C_3N_4	2.71	10.88
MOF@DF-C_3N_4	2.65	11.49
Nano-MOF-74	2.63	—

nitrogen vacancies, which results in the introduction of defect bands ($V_N^{\cdots}$) under the conduction band (CB). At the same time, it can be seen from Fig. S7† that the absorption edges for F-C_3N_4 and DF-C_3N_4 blue-shift compared with bulk C_3N_4, which corresponding to the color change from pale yellow to deep yellow. The color of Nano-MOF is also lighter than that of bulk MOF-74. As can be seen from the fluorescence spectra in Fig. 5c, the MOF@F-C_3N_4 or MOF@DF-C_3N_4 composites basically did not change the fluorescence absorption compared with F-C_3N_4 or DF-C_3N_4, respectively. However, compared with F-C_3N_4, the fluorescence of DF-C_3N_4 was significantly reduced. The decrease of fluorescence emission indicates that the recombination of photogenic carriers is significantly reduced. This fact can be explained by that nitrogen vacancies in DF-C_3N_4 can trap electrons and effectively reduce the recombination of electrons and holes, thus improving the photocatalytic activity of nitrogen fixation. The PL emission wavelength for DF-C_3N_4 (475 nm equals to 2.61 eV) is higher than that for F-C_3N_4 (465 nm equals to 2.67 eV), which is in good accordance with the band gap obtained from UV-Vis spectra (Table 1). The transient PL decay spectra in Fig. 5d further gives us evident to explain the photocatalytic nitrogen fixation activities. The average PL lifetimes of bulk C_3N_4, F-C_3N_4, DF-C_3N_4, MOF@F-C_3N_4 and MOF@DF-C_3N_4 were calculated to be 9.65, 11.92, 12.44, 10.88 and 11.49 ns, respectively. Compared with pure F-C_3N_4, the relaxation life of pure DF-C_3N_4 increases, which implies DF-C_3N_4 with nitrogen defects has a strong trapping ability for electrons to increase the relaxation life.[40] While for MOF@F-C_3N_4 or MOF@DF-C_3N_4 composites, the relaxation lives decrease compared with pure F-C_3N_4 or pure DF-C_3N_4 respectively. This result can be explained by the formation of Z-scheme heterojunction (as described in the next paragraph) leading to high efficiency of charge separation.[41] Average relaxation life can be used as an index to evaluate the efficiency of charge separation: the faster the relaxation, the higher the efficiency.[42] The fast relaxation life of MOF@DF-C_3N_4 thus corresponds to the large photogenic carrier separation and the high ammonia production.[43]

$$N_2 + 8H^+ + 8e^- \rightarrow 2NH_4^+,\ 0.27\ eV \quad (2)$$

Fig. 6a shows the bandgap structures of F-C_3N_4, Nano-MOF-74 and DF-C_3N_4. The energies of valence bands (VB) of the three are obtained from XPS valence band spectra (Fig. S8†). Then according to E_g results obtained from UV-Vis spectra (Table 1), the energies of conduction bands can be calculated. The electric potential required for N_2 conversion to NH_4^+ is +0.27 eV (eqn (2)),[39] and the conduction band of Nano-MOF-74 is located at +0.77 eV. Thus the electrons on the CB of Nano-MOF-74 cannot cause N_2 convert to NH_4^+, so we speculate that the combination of Nano-MOF-74 with F-C_3N_4 or DF-C_3N_4 results in a Z-scheme heterojunction (Fig. 6b). It is beneficial to the application of semiconductor heterostructure in photocatalysis if the photocarrier separation can be realized while maintaining their redox ability. In the semiconductor heterogeneous structure formed by Nano-MOF-74 and DF-C_3N_4, the photogenic electrons on the CB of Nano-MOF-74 transfer and recombine with the photogenic holes on the VB of DF-C_3N_4 at the interface. Thus, the photogenic electrons on the CB of DF-C_3N_4 with stronger reduction capacity and the photogenic holes on the VB of Nano-MOF-74 with stronger oxidation capacity were retained, this is a typical vector Z mechanism carrier transfer. To be sure, in the mechanism of the semiconductor heterostructure, the traditional type II carrier transfer process (the electrons transfer from high CB of DF-C_3N_4 to low CB of Nano-MOF-74) can still happen (Fig. 6c), it can be seen that the electron should be transferred from the conduction band of DF-C_3N_4 to the conduction band of Nano-MOF-74, while the hole is transferred from the valence band of Nano-MOF-74 to the valence band of DF-C_3N_4. The two carrier transfer processes (Z-scheme and type II) are competitive. The results of our fluorescence lifetime test

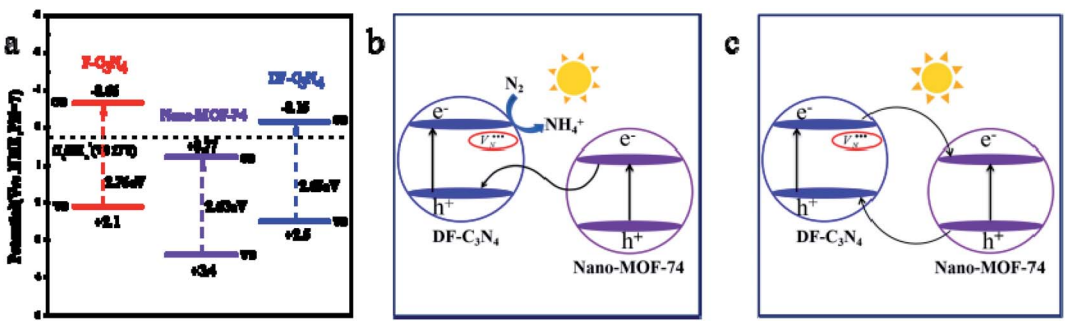

Fig. 6 (a) The bandgap structures of F-C_3N_4, Nano-MOF-74 and DF-C_3N_4; (b) charge separation process with Z-scheme mechanism on MOF@DF-C_3N_4. (c) Charge separation process with the traditional type II mechanism.

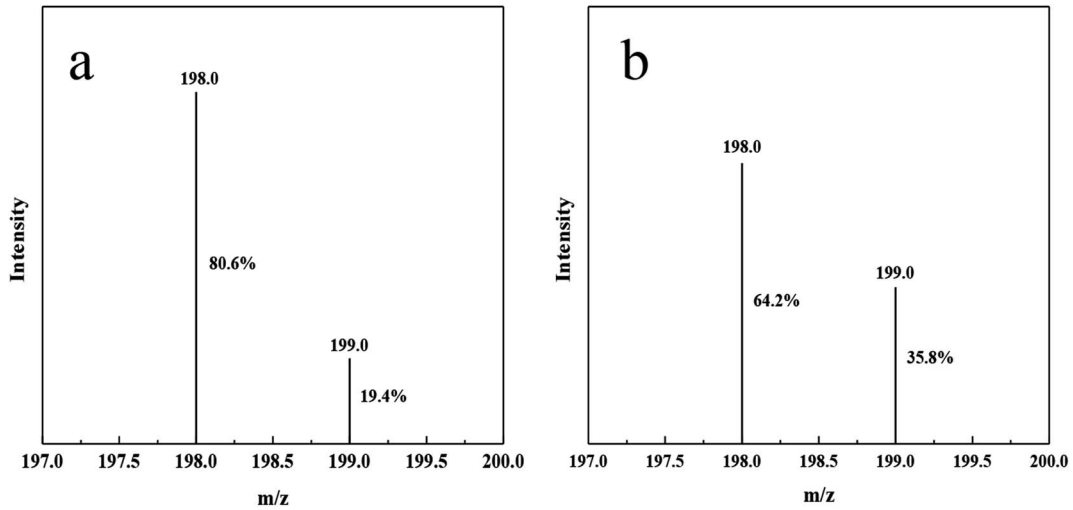

Fig. 7 The mass spectra of the indophenol prepared from different atmosphere. (a) The mass spectra of the indophenol prepared from $^{14}N_2$ atmosphere; (b) the mass spectra of the indophenol prepared from $^{15}N_2$ atmosphere.

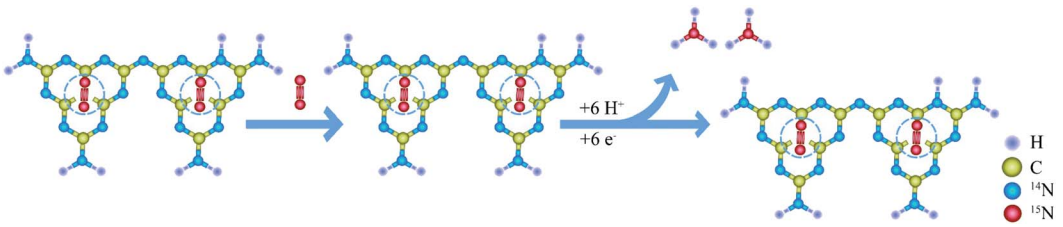

Scheme 2 The reaction of ^{15}N labeled $^{15}N_2$ to ammonia nitrogen catalyzed by DF-C_3N_4.

support the Z-scheme for MOF@DF-C_3N_4 composite, and the position of its conduction band is higher with higher electronic reduction capability, so we believe that the mechanism is mainly Z-scheme instead of type-II scheme. Therefore, nitrogen defects introduced in DF-C_3N_4 play an important role. Electrons were captured by the nitrogen defects and prevented the electron transfer from the CB of DF-C_3N_4 to the CB of Nano-MOF-74. In this way, the concentration of photogenic carriers is increased, and the photocatalytic activity of nitrogen fixation is improved.

In order to prove that the nitrogen source of ammonia nitrogen products generated by photocatalysis comes from nitrogen, we made isotopic labeling of $^{15}N_2$. Vacuumed the reactor to change nitrogen, replaced $^{14}N_2$ with $^{15}N_2$, and then let it stand for 12 hours. Then, normal photocatalytic reaction was carried out, and the product after the reaction was taken for indophenol method. Through LC-MS analysis, compared with ^{14}N indophenol blue, the content of ^{15}N indophenol blue increased by 16.4% (Fig. 7).The reaction process is shown in the Scheme 2, ^{15}N labeled $^{15}N_2$ is adsorbed to the N defects on DF-C_3N_4, and after contact with photogenic electrons, the nitrogen–nitrogen triple bond breaks, and ammonia nitrogen products are generated contact with hydrogen ions.[44] So during the process, the nitrogen on DF-C_3N_4 is not involved in the formation of ammonia, and the nitrogen source in ammonia nitrogen come from the N_2.

3. Conclusion

In summary, we successfully combined nano-sized Nano-MOF-74 (Zn) with nitrogen-defected thin film C_3N_4. The experimental results showed that nitrogen fixation activity of the composite was effectively improved compared with pure DF-C_3N_4 under visible light irradiation. We speculated that this was mainly due to the formation of Z-scheme heterojunction, which reduced the photogenic carrier recombination. Further, the presence of nitrogen defects can prevent the electron transfer and effectively improve the concentration of photogenic carriers. This provides a new idea for the future work on the combination of MOFs and inorganic materials, and provides a new thought for improving the photoactivity of visible light nitrogen fixation.

4. Experimental procedures

2,5-dihydroxy terephthalic acid (2,5-BDC) was purchased from Meryer, $Zn(NO_3)_2 \cdot 6H_2O$ was purchased from Aladdin, *N*,*N*-dimethylformamide (DMF) was purchased from FoChen, melamine was purchased from Kermel, triethylamine and deionized (DI) water were purchased from ConCord. All

chemical reagents are A.R grade and are not further purified after purchase from reagent company.

4.1 Synthesis of photocatalyst

Bulk C_3N_4. Put melamine into the muffle furnace and increased the temperature to 550 °C at a rate of 2.5 °C per minute, calcined for 2 hours and natural cooled to room temperature.

Tube C_3N_4. As reported in previous literature,[45] 1 g melamine and 1.2 g phosphorous acid were dissolved in 100 ml deionized water at 80 °C in thermostatic water bath with strong stirring for 1 h. Then the solution was transferred to the Teflon reaction liner and heated at 180 °C for 10 hours. The solid products was centrifuged, washed five times with deionized water to remove other impurities. Finally, the tube-shaped precursor was obtained by vacuum drying at 60 °C for 10 hours. The tube-shaped precursor was kept in muffle furnace for two hours at a heating rate of 2 °C min^{-1} to 500 °C and the tube C_3N_4 was obtained after natural cooling.

Film C_3N_4. 0.6 g tube C_3N_4 was added into the mixed solution of 5 ml glycerol and 15 ml ethanol for reflux at 100 °C for 3 hours. Then the powder was centrifuged, washed with ethanol for 5 times and then dried at 60 °C. Finally, the dried powder was put into the muffle furnace and calcined for 2 hours after heating up to 500 °C at a heating rate of 2 °C min^{-1}. Product film C_3N_4 was obtained after natural cooling and denoted as F-C_3N_4.

Defected C_3N_4. A certain amount of F-C_3N_4 was put into a tubular furnace. Under the protection of nitrogen, the temperature was increased to 520 °C with a rate of 20 °C min^{-1} and kept for 2 hours to obtain the defected C_3N_4 (denoted as DF-C_3N_4).

Nano-MOF-74(Zn). 0.1 g 2,5 dihydroxy terephthalic acid (2,5-BDC) and 0.452 g $Zn(NO_3)_2 \cdot 6H_2O$ were dissolved in 200 ml DMF solvent and magnetically stirred until the solid was completely dissolved. Then added 10 ml of deionized water dropwised into the solution until full mix. Whereafter, 1 ml triethylamine was dropwised into the solution and form a pale yellow precipitate (Scheme S1†). After centrifugation, the powder was dried at 130 °C and then washed with deionized water and ethanol for 3 times respectively. Finally, the powder was put into a tubular furnace and heated up to 200 °C for 2 hours under nitrogen protection at the rate of 10 °C min^{-1}.

Nano-MOF-74(Zn)@film-C_3N_4. 20 mg Nano-MOF-74(Zn) and 80 mg F-C_3N_4 were added to 100 ml ethanol for ultrasound for 1 h respectively, then the suspension solution of Nano-MOF-74 was simultaneously added to the F-C_3N_4 solution for another 1 h with ultrasound. The ultrasonic suspension was rested for one night to obtain the upper liquid. After extraction with dropper, the remaining precipitation was dried at 60 °C for 10 hours. The dried powder was put into a tubular furnace and calcined for 2 hours at 200 °C under the protection of nitrogen to make its combination more stable. Finally, it was denoted as MOF@F-C_3N_4.

Nano-MOF-74(Zn)@DF-C_3N_4. The synthesis process is like that of Nano-MOF-74(Zn)@F-C_3N_4, except that F-C_3N_4 is replaced by DF-C_3N_4, and the other processes are the same. The product is denoted as MOF@DF-C_3N_4.

4.2 Characterization

With 10° min^{-1} scanning rate, powder X-ray diffraction (XRD) patterns were recorded in the range 3° to 80° on a Rigaku MiniFlex 600 using CuKα radiation ($\lambda = 0.154178$ nm) at 298 K. Electrochemical data testing was performed at the Chenhua CHI 760E electrochemical workstation. The samples' morphologies were analyzed through JSM-7800F scanning electron microscope (SEM). Using a JEM-2800 microscope high-resolution TEM (HRTEM) images were tested. The UV-Vis measurement of the samples was carried out by a spectrophotometer with TU-1950 PERSEE. Steady-state fluorescence spectra were measured by HITACHI F-7000. The measurement of fluorescence lifetime was performed by FLS920 transient fluorescence/phosphorescence spectrometer (77–500 K). Atomic force microscope (AFM, Bruker Dimension Icon) was used to measure the thickness of samples. Magnetic susceptibility measurements were performed with MPMS3 from Quantum Design. The data were measured from 300 K to 250 K at 1000 Oe direct-current field. Data were corrected for the diamagnetic contribution calculated from Pascal constants. Unpaired electrons were detected using an ESR spectrometer (EMX plus-6/1) at room temperature.

4.3 Photocatalytic N_2 reduction reaction measurements

Photocatalytic nitrogen fixation reaction is carried out in Zhong Jiao Jin Yuan photocatalytic reactor (CEL-APR100H). 10 mg photocatalyst was added to the mixed solution of 48 ml H_2O and 2 ml methanol (as the hole trapping agent) for 15 min ultrasound, and then transferred to the photocatalytic reactor for sealing. The reactor controlled the reaction temperature at 25 °C by circulating condensed water and the reaction was carried on under atmospheric pressure with magnetic stirring. The light source is 300 W Xe lamp (CEL-HXF300) about 15 cm away from the photocatalytic reactor with a cut-off filter (400 nm) for visible-light photocatalysis. During the illumination, 1 ml solution was taken every half an hour to detect NH_4^+ content by the Nessler reagent method at 420 nm with an ultraviolet spectrophotometer (KU-T6PC).

4.4 Photocurrent experiments

10 mg samples were dispersed in 1 ml ethanol for half an hour by ultrasound, and the samples were uniformly coated on ITO glass with the area of 1 × 1 cm. Then vacuum dried the conductive glass coated with the sample for 10 h to make the sample and conductive glass combine more firmly. The photocurrent test was carried out in a quartz pool with ITO conductive glass coated with the sample as the working electrode, a Pt foil as counter electrode and an Ag/AgCl electrode as reference electrode, and the electrolyte was Na_2SO_4 (0.1 M) aqueous solution. In visible light photocurrent tests, the ultraviolet light is filtered out using a 400 nm filter under a 300 W Xe lamp.

The electrochemical impedance spectra (EIS) were recorded when the initial voltage is open circuit voltage over the frequency range of 1 MHz to 1 Hz under illumination condition.

4.5 N-15 labeling experiments

The catalyst and sacrificial agent of the same amount as the normal photocatalytic reaction were added to 48 ml water for 10 min after ultrasonic treatment, and then poured into the reactor. A circulating water pump was used to vacuum the reactor and replace $^{14}N_2$ with $^{15}N_2$. After 2 hours of reaction, 0.5 ml of the reaction liquid filtered through the filter membrane was taken and mixed with 0.1 ml of 1% phenolic solution in 95% ethanol/water, 0.375 ml of 1% NaClO in alkaline Na-citrate solution in water and 0.5 ml of 0.5% Na $[Fe(CN)_5NO]$ in water for reaction. After 12 hours until fully developed, it was tested by LC-MS.[46]

Conflicts of interest

There are no conflicts to declare.

Acknowledgements

This work was partly supported by Natural Science Foundation of China (21576140) and Natural Science Foundation of Tianjin (17JCYBJC20000, 19JCTPJC46300).

References

1 B. K. Burgess and D. J. Lowe, Mechanism of Molybdenum Nitrogenase, *Chem. Rev.*, 1996, (7), 2983–3012.
2 R. Chandra and M. J. C. Nath, Multi-Core–shell TiO_2 NPs@ZIF-8 Composite for Enhanced Photocatalytic Degradation and Adsorption of Methylene Blue and Rhodamine-B, *ChemistrySelect*, 2017, **2**(25), 7711–7722.
3 S. Chen, T. Takata and K. J. N. R. M. Domen, Particulate photocatalysts for overall water splitting, *Nat. Rev. Mater.*, 2017, **2**, 17050.
4 S. Cong, Y. Yuan, Z. Chen, J. Hou, M. Yang, Y. Su, Y. Zhang, L. Li, Q. Li and F. Geng, Noble metal-comparable SERS enhancement from semiconducting metal oxides by making oxygen vacancies, *Nat. Commun.*, 2015, **6**(6–7), 7800.
5 J. W. Erisman, M. A. Sutton, J. Galloway, *et al.*, How a century of ammonia synthesis changed the world, *Nat. Geosci.*, 2008, **1**(10), 636–639.
6 H. Guo, D. Guo, Z. Zheng, *et al.*, Visible-light photocatalytic activity of Ag@MIL-125(Ti) microspheres, *Appl. Organomet. Chem.*, 2015, **29**(9), 618–623.
7 H. Hirakawa, M. Hashimoto, Y. Shiraishi, *et al.*, Photocatalytic Conversion of Nitrogen to Ammonia with Water on Surface Oxygen Vacancies of Titanium Dioxide, *J. Am. Chem. Soc.*, 2017, **139**(31), 10929–10936.
8 K. Honkala, A. Hellman, I. N. Remediakis, *et al.*, Ammonia Synthesis from First-Principles Calculations, *Science*, 2005, **307**(5709), 555–558.
9 L. Jiang, L. Y. Sun, X. D. Pan, *et al.*, Characterization of the unique Chinese W483X mutation in the low-density lipoprotein (LDL)-receptor gene in young patients with homozygous familial hypercholesterolemia, *J. Clin. Lipidol.*, 2015, **10**(3), 538–546.e5.
10 X. Cao, C. Li, Y. Li, *et al.*, Enhanced performance of perovskite solar cells by modulating Lewis acid-base reaction, *Nanoscale*, 2016, 19804–19810.
11 J. Li, H. Li, G. Zhan, *et al.*, Solar Water Splitting and Nitrogen Fixation with Layered Bismuth Oxyhalides, *Acc. Chem. Res.*, 2017, **50**(1), 112–121.
12 X. Li, J. Iocozzia, Y. Chen, *et al.*, Functional Nanoparticles Enabled by Block Copolymer Templates: from Precision Synthesis of Block Copolymers to Properties and Applications of Nanoparticles, *Angew. Chem.*, 2017, 2046–2070.
13 X. Deng, L. Yang, H. Huang, *et al.*, Shape-Defined Hollow Structural Co-MOF-74 and Metal Nanoparticles@Co-MOF-74 Composite through a Transformation Strategy for Enhanced Photocatalysis Performance, *Small*, 2019, e1902287.
14 C. Xu, Y. Pan, G. Wan, H. Liu, L. Wang, H. Zhou, S. H. Yu and H. L. Jiang, Turning on Visible-Light Photocatalytic C-H Oxidation over Metal-Organic Frameworks by Introducing Metal-to-Cluster Charge Transfer, *J. Am. Chem. Soc.*, 2019, **141**(48), 19110–19117.
15 T. He, B. Ni, S. Zhang, *et al.*, Ultrathin 2D Zirconium Metal–Organic Framework Nanosheets: Preparation and Application in Photocatalysis, *Small*, 2018, **14**, 1703929.
16 V. Singh, I. J. C. Beltran, J. C. Ribot and P. Nagpal, Photocatalysis Deconstructed: Design of a New Selective Catalyst for Artificial Photosynthesis, *Nano Lett.*, 2014, **14**(2), 597–603.
17 N. L. Rosi, J. Kim, M. Eddaoudi, B. Chen, M. O'Keeffe and O. M. Yaghi, Rod Packings and Metal–Organic Frameworks Constructed from Rod-Shaped Secondary Building Units, *J. Am. Chem. Soc.*, 2005, **127**(5), 1504–1518.
18 L. Valenzano, B. Civalleri, S. Chavan, G. T. Palomino, C. O. Areán and S. Bordiga, Computational and Experimental Studies on the Adsorption of CO, N_2, and CO_2 on Mg-MOF-74, *J. Phys. Chem. C*, 2010, **114**(25), 11185–11191.
19 J. D. Xiao and H. L. Jiang, Thermally Stable Metal-Organic Framework-Templated Synthesis of Hierarchically Porous Metal Sulfides: Enhanced Photocatalytic Hydrogen Production, *Small*, 2017, 1700632.
20 Y. Z. Chen, B. Gu, T. Uchida, J. Liu, X. Liu, B. J. Ye, Q. Xu and H. L. Jiang, Location determination of metal nanoparticles relative to a metal-organic framework, *Nat. Commun.*, 2019, **10**(1), 3462.
21 J. W. F. To, J. He, J. Mei, *et al.*, Hierarchical N-Doped Carbon as CO_2 Adsorbent with High CO_2 Selectivity from Rationally Designed Polypyrrole Precursor, *J. Am. Chem. Soc.*, 2015, **138**(3), 1001–1009.
22 J. L. C. Rowsell and O. M. Yaghi, Effects of Functionalization, Catenation, and Variation of the Metal Oxide and Organic Linking Units on the Low-Pressure Hydrogen Adsorption

Properties of Metal Organic Frameworks, *J. Am. Chem. Soc.*, 2006, **128**(4), 1304–1315.

23 D. A. Giannakoudakis, N. A. Travlou, J. Secor, *et al.*, Oxidized g-C_3N_4 Nanospheres as Catalytically Photoactive Linkers in MOF/g-C_3N_4 Composite of Hierarchical Pore Structure, *Small*, 2016, **13**(1), 1601758.

24 X. Zhang, X. Xie, H. Wang, *et al.*, Enhanced Photoresponsive Ultrathin Graphitic-Phase C_3N_4 Nanosheets for Bioimaging, *J. Am. Chem. Soc.*, 2012, **135**, 18–21.

25 X. Zhang, H. Wang, H. Wang, Q. Zhang, J. Xie, Y. Tian, J. Wang and Y. Xie, Single-Layered Graphitic-C_3N_4 Quantum Dots for Two-Photon Fluorescence Imaging of Cellular Nucleus, *Adv. Mater.*, 2014, **26**(26), 4438–4443.

26 Q. Liu, L. Ai and J. Jiang, MXene-derived TiO_2@C/g-C_3N_4 heterojunctions for highly efficient nitrogen photofixation, *J. Mater. Chem. A*, 2018, **6**, 4102–4110.

27 W. Tang, X. Wu and Y. Chen, Catalytic removal of gaseous benzene over Pt/SBA-15 catalyst: the effect of the preparation method, *React. Kinet., Mech. Catal.*, 2015, **114**(2), 711–723.

28 Q. Liao, Z. Xie, B. Pan, *et al.*, LC–MS–MS Simultaneous Determination of Paracetamol, Pseudoephedrine and Chlorpheniramine in Human Plasma: Application to a Pharmacokinetic Study, *Chromatographia*, 2008, **67**(s. 9–10), 687–694.

29 R. Wang, L. Gu, J. Zhou, *et al.*, Quasi-Polymeric Metal–Organic Framework UiO-66/g-C_3N_4 Heterojunctions for Enhanced Photocatalytic Hydrogen Evolution under Visible Light Irradiation, *Adv. Mater. Interfaces*, 2015, **2**, 1500037.

30 G. Liu, W. Tao, *et al.*, Nature-Inspired Environmental "Phosphorylation" Boosts Photocatalytic H2 Production over Carbon Nitride Nanosheets under Visible-Light Irradiation., *Angew. Chem.*, 2015, **127**(46), 13765–13769.

31 H. Guo, F. Lin, J. Chen, *et al.*, Metal-organic framework MIL-125(Ti) for efficient adsorptive removal of Rhodamine B from aqueous solution, *Appl. Organomet. Chem.*, 2015, **29**(1), 12–19.

32 C. Bai, J. Bi, J. Wu, *et al.*, Fabrication of noble-metal-free g-C_3N_4-MIL-53(Fe) composite for enhanced photocatalytic H_2-generation performance, *Appl. Organomet. Chem.*, 2018, **32**, e4597.

33 C. C. Wang and Y. S. Ho, Research trend of metal–organic frameworks: a bibliometric analysis, *Scientometrics*, 2016, **109**(1), 481–513.

34 S. D. Han, W. C. Song, J. P. Zhao, *et al.*, Synthesis and ferrimagnetic properties of an unprecedented polynuclear cobalt complex composed of [Co_(24)] macrocycles, *Chem. Commun.*, 2013, **49**(9), 871–873.

35 H. Fu, Z. Wang, W. Xun, W. Peng and C. C. Wang, Formation mechanism of rod-like ZIF-L and fast phase transformation from ZIF-L to ZIF-8 with morphology changes controlled by polyvinylpyrrolidone and ethanol, *CrystEngComm*, 2018, **20**(11), 1473–1477.

36 J. Liu, Y. Liu, N. Liu, *et al.*, Metal-free efficient photocatalyst for stable visible water splitting via a two-electron pathway, *Science*, 2015, **347**(23), 970–974.

37 G. Gao, Y. Jiao, F. Ma, *et al.*, Carbon nanodot decorated graphitic carbon nitride: new insights into the enhanced photocatalytic water splitting from ab initio studies, *Phys. Chem. Chem. Phys.*, 2015, **17**(46), 31140–31144.

38 G. Dong, W. Ho and C. Wang, Selective photocatalytic N_2 fixation dependent on g-C_3N_4 induced by nitrogen vacancies, *J. Mater. Chem. A*, 2015, **3**(46), 23435–23441.

39 S. Yasuhiro, *et al.*, Nitrogen Fixation with Water on Carbon-Nitride-Based Metal-Free Photocatalysts with 0.1% Solar-to-Ammonia Energy Conversion Efficiency, *ACS Appl. Energy Mater.*, 2018, 8b00829.

40 P. Qiu, C. Xu and N. Zhou, Metal-free black phosphorus nanosheets-decorated graphitic carbon nitride nanosheets with C-P bonds for excellent photocatalytic nitrogen fixation, *Appl. Catal., B*, 2018, **221**, 27–35.

41 H. L. Jiang, X. Ma, L. Wang, *et al.*, Switching on Photocatalysis of Metal–Organic Frameworks by Engineering Structural Defects, *Angew. Chem.*, 2019, **131**(35), 12303–12307.

42 H. Diarmand-Khalilabad, A. Habibi-Yangjeh, D. Seifzadeh, *et al.*, g-C_3N_4 nanosheets decorated with carbon dots and CdS nanoparticles: Novel nanocomposites with excellent nitrogen photofixation ability under simulated solar irradiation, *Ceram. Int.*, 2018, **45**(2), 2542–2555.

43 H. Wang, *et al.*, MIL-100(Fe)/Ti_3C_2 MXene as a Schottky Catalyst with Enhanced Photocatalytic Oxidation for Nitrogen Fixation Activities, *ACS Appl. Mater. Interfaces*, 2019, **11**(47), 44249–44262.

44 C. Lv, Y. Qian, C. Yan, *et al.*, Defect Engineering Metal-Free Polymeric Carbon Nitride Electrocatalyst for Effective Nitrogen Fixation under Ambient Conditions, *Angew. Chem.*, 2018, **130**(32), 10403–10407.

45 G. Li, *et al.*, Fe-based MOFs for photocatalytic N_2 reduction: Key role of transition metal iron in nitrogen activation, *J. Solid State Chem.*, 2020, **285**, 121245.

46 S. J. Geromanos, J. P. Vissers, J. C. Silva, *et al.*, The detection, correlation, and comparison of peptide precursor and product ions from data independent LC-MS with data dependant LC-MS/MS, *Proteomics*, 2009, **9**(6), 1683.